A hybrid LES-RANS validation of effusion cooling array measurements

Xiaosheng Chen*
Hao Xia

Department of Aeronautical and Automotive Engineering
Loughborough University
Loughborough
UK

ABSTRACT

In this work, an effusion cooling array is studied using a hybrid LES-RANS approach under combustor representative conditions. The surface adiabatic cooling effectiveness is examined. Promising results are obtained from the hybrid LES approach based on an 18-million-cell grid. The turbulent flow field is studied in order to investigate the effects on the coolant-mainstream mixing, as well as the distribution of the coolant film. It is found that the free-stream turbulence leads to early breakdown of the coolant jets at the 1st and 2nd row of coolant holes, while such effects diminish in the downstream region due to the turbulent structures in the mixed mainstream. As a result, the surface adiabatic cooling effectiveness stays low in the first few rows, but keeps growing and reaches a high value in the downstream rows.

* x.chen@lboro.ac.uk

1.0 Introduction

Effusion cooling is a commonly used technology to protect jet engine components such as combustor liners and turbine blades from the hot gas. By injecting coolant through an effusion cooling array, a film of low temperature air is formed on the solid surface to isolate it from the high temperature gas. Increasing the coverage of the coolant film improves the cooling effect but simply increasing the amount of coolant reduces the efficiency of jet engine components. Therefore, good understanding of the effusion cooling mechanism is critical for enhancing the cooling effect with minimum coolant usage.

One of the most frequently investigated effusion cooling configurations consists of a single row of injection holes with a length to diameter ratio of 1.75 or 3.5, an inclination angle of 35° to the mainstream, and a spanwise hole distance of 3 diameters. A series of experiments were carried out by Sinha and others[1,2,3,4]. Numerical simulations of this configuration using the Reynolds-averaged Navier-Stokes (RANS) approach have been performed by many groups[5,6,7]. Although these RANS studies were generally able to reproduce the time-mean flow quantities with reasonable accuracy, a time-dependent approach such as Large-Eddy Simulation (LES) offers great advantages in resolving the unsteady structures of the mixing flow as the mixing of the coolant and mainstream is dominated by secondary flows and vortex interactions. Several groups have conducted LES studies on single-row configurations and obtained good agreement with experimental data[8,9,10]. Ziefle and Kleiser[11] carried out an LES study with turbulent inflow for the mainstream. Considerable differences in the cooling effectiveness distribution were found compared to those without inflow turbulence.

Effusion cooling array configurations with a turbulent inflow were studied experimentally by Martin[12] and Krawciw et al.[13] under combustor representative conditions. This is an ideal case for testing the numerical model. However, the near-wall grid points required for fully wall resolved LES are proportional to Re^2, nearly as many as for Direct Numerical Simulation (DNS). This makes the wall-resolved LES very expensive especially at high Reynolds number cases such as the experiments by Krawciw et al.[13]. Therefore, the near wall boundary layer needs some kind of treatment and RANS seems highly suitable among many other options. In the present study, we apply a hybrid LES-RANS approach for the validation of the effusion cooling array measurements under the combustor representative conditions[13].

2.0 Methodology

The Favre-averaged compressible Navier-Stokes equations for ideal gas are solved in conservation form,

$$\frac{\partial \overline{\mathbf{Q}}}{\partial t} + \frac{\partial \overline{\mathbf{F}}_i^{inv}}{\partial x_i} - \frac{\partial \overline{\mathbf{F}}_i^{vis}}{\partial x_i} = 0 \qquad \ldots(1)$$

The conservative variables are $\overline{\mathbf{Q}} = [\overline{\rho}, \overline{\rho}\widetilde{u_i}, \widetilde{E}]^T$, the inviscid and viscous fluxes are defined as $\overline{\mathbf{F}}_i^{inv} = \widetilde{u_i}\overline{\mathbf{Q}} + [0, \delta_{1i}\overline{p}, \delta_{2i}\overline{p}, \delta_{3i}\overline{p}, \widetilde{u_i}\overline{p}]^T$ and $\overline{\mathbf{F}}_i^{vis} = [0, \widetilde{\tau}_{1i}, \widetilde{\tau}_{2i}, \widetilde{\tau}_{3i}, \widetilde{\tau}_{ki}\widetilde{u}_k + \widetilde{q}_i]^T$. The stress tensor $\widetilde{\tau}_{ij}$, total energy $\widetilde{E}$ and heat flux $\widetilde{q}_j$ satisfies,

$$\widetilde{\tau}_{ij} = 2(\mu + \mu_T)\left(\widetilde{S}_{ij} - \frac{1}{3}\partial_k \widetilde{u}_k \delta_{ij}\right), \quad \widetilde{E} = \overline{\rho e} + \frac{1}{2}\overline{\rho}\widetilde{u_i}\widetilde{u_i}, \quad \widetilde{q}_i = -(\kappa + \kappa_T)\frac{\partial \widetilde{T}}{\partial x_i} \qquad \ldots(2)$$

where the turbulent thermal conductivity is computed from $\kappa_T = \mu_T c_p / Pr_T$. An extra equation of state $\overline{p} = \overline{\rho} R \widetilde{T}$ is also included.

2.1 LES-RANS hybridisation

In this work, a wall proximity is used to control the destruction of the eddy viscosity in RANS. This is different from the Detached Eddy Simulation (DES), where the approximate turbulent lengthscale is replaced by the weighting between the lengthscale and grid spacing $\min(L_T, C_{DES}\Delta)$[14]. In these circumstances, the interface between the LES and RANS in the DES is not fixed but depending on the flow and grid resolution. However, in our hybrid LES-RANS approach, the LES-RANS interface is determined at a given wall distance. And the LES and RANS regions are defined by a modified wall distance,

$$\widetilde{d} = \left[1 - \tanh\left(\alpha \frac{d - d_c}{d_c}\right)\right] \frac{d}{2} \quad \ldots(3)$$

where α is a coefficient to control the decay rate of $\widetilde{d}$ in the mixed zone, d_c is the RANS cut-off distance typically at $y^+ \sim 60$. The weighting parameter for LES is defined as,

$$\varepsilon = \tanh\left[\beta(d - \widetilde{d})\right] \quad \ldots(4)$$

where β is a coefficient that controls the growth of ε in the mixed zone.

In the SST model, the turbulent lengthscale L_T in the destruction term Y_k of the transport equation is modified based on the ratio between the wall distance and modified wall distance $\widetilde{d}/d$ to control the LES-RANS blending,

$$Y_k = k^{3/2} \frac{d}{L_T \widetilde{d}} \quad \ldots(5)$$

The turbulent length scale L_T therefore scales with the modified wall distance in the mixed zone, but returns to the original value in the RANS zone.

As Fig. 1 shows, the RANS and LES regions are defined based on the modified wall distance $\widetilde{d}$. The eddy viscosity of RANS reduces when moving away from the wall in the mixed zone. The weighting of LES increases in the mixed zone when ε gradually increases from 0. In the LES region, the eddy viscosity of RANS vanishes, and $\varepsilon = 1$ if an explicit SGS model is used. A smooth transition in the eddy viscosity field is therefore obtained and helps to maintain good numerical stability.

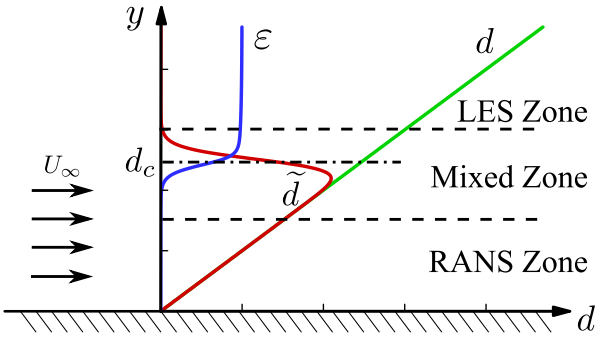

Figure 1: Blending of RANS and LES regions

This hybrid LES-RANS approach has been successfully applied to various studies, such as chevron jets[15,16] and a heated square cylinder in cross-flow[17]. In this work no explicit SGS model is used ($\varepsilon = 0$), which is often referred to as implicit or numerical LES.

2.2 Spatial and temporal discretisation

Viscous terms are discretised using the central differencing scheme, while a MUSCL type reconstruction with a modified Roes scheme is used for inviscid fluxes at the common face of two neighbouring cells,

$$\mathbf{F} = \frac{1}{2}(\mathbf{F}_R + \mathbf{F}_L) - \frac{\gamma}{2}\left|\frac{\partial \mathbf{F}}{\partial \mathbf{Q}}\right|(\mathbf{Q}_R - \mathbf{Q}_L) \quad \ldots(6)$$

where the up-winding term is controlled by parameter $\gamma \in (0, 1]$. Central difference is used for accurately resolving the turbulent structures when $\gamma = 0$, while the upwinding term is fully functioning for numerical stability when $\gamma = 1$. $\mathbf{Q}$ and $\mathbf{F}$ are the conservative and flux vectors. Subscripts L and R represent the immediate left and right position of the common flux face, where piecewise linear reconstructions are performed from cell centres to give a second-order spatial accuracy. Moreover, the dual-time advancing is employed with the outer physical time discretised by a three-level backward Euler scheme, thus leading to a second-order temporal accuracy. The inner pseudo time is advanced by a three-stage Runge-Kutta scheme. As the outer time is discretised implicitly, it allows larger physical time steps to increase the efficiency compared with explicit time marching.

3.0 Configuration

3.1 Computational domain and boundary conditions

A sketch of the computational domain is illustrated in Fig. 2. It contains only two columns of cylindrical coolant holes with a diameter noted as D. Using the periodic boundary conditions at the two sides of the mainstream channel, this section can be extended periodically in the spanwise direction, mimicking the full plate in experiments[13]. The top surface of the main channel locates at about 7.75 D away from the plate surface, and it is defined as far-field to allow flow penetration through the boundary. The origin of the computational domain is set at the centre of the two rows and parallel to the leading edge of the first coolant hole. The inlet locates at about 11.6 D away from the leading edge of the first hole and the outlet is at about 15 D away from the trailing edge of the last hole. The bottom surface of the main channel, together with the coolant hole surface and top surface of the coolant chamber, is set as no-slip and zero heat flux wall. This ensures that no extra heat is introduced to the domain and that the wall surface is adiabatic. In this way, the measured cooling effectiveness is referred to as the adiabatic cooling effectiveness (ACE) following the equation below,

$$\eta = \frac{T_\infty - T_w}{T_\infty - T_c} \quad \ldots(7)$$

where T_∞ is the mainstream temperature, T_w is the adiabatic wall temperature and T_c is the coolant temperature. The coolant enters the chamber from the bottom surface that is about 4.65 D away from the coolant hole inlet. The surfaces of 4 sides are slip walls to make sure that all the coolant that enters the chamber will come out from the coolant holes.

The mainstream bulk velocity is $U_\infty = 36\ m/s$ with a velocity profile specified at the inlet. The coolant speed at the inlet of the chamber is adjusted so that a bulk velocity of about $U_c = 51.43\ m/s$ is reached at the coolant hole exit. The mainstream temperature is $T_\infty = 315\ k$ while the coolant flow has a temperature of about $T_c = 300\ K$. This leads to a density ratio of

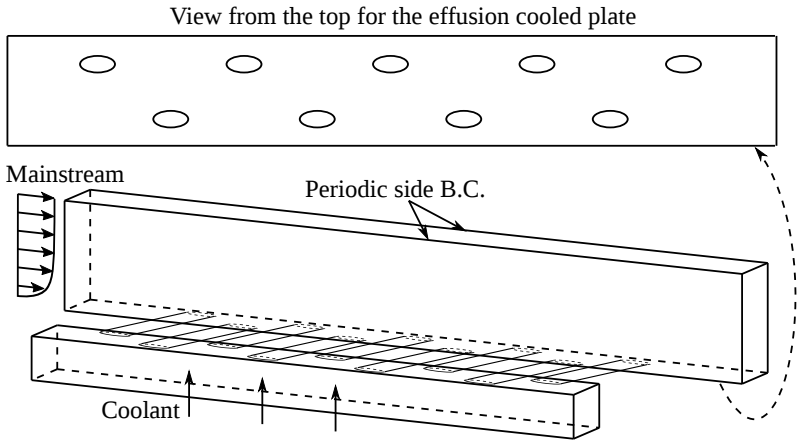

Figure 2: A sketch of the computational domain and boundaries

1.05, which is consistent with the conditions in experiments[13]. Such conditions result in the blowing ratio to be $BR = 1.5$, and the momentum ratio to be $MR = 2.14$.

A velocity profile is used at the inlet of the mainstream with synthetically generated free-stream turbulence by SEM. Free-stream turbulence is introduced to the inflow using the Synthetic Coherent Eddy Method (SCEM)[18] with an intensity level of 5%, following the level in the experiments[13].

3.2 Computational grids

An unstructured grid of 18-million cells is generated for the multi-row effusion cooling simulations as Fig. 3 shows. Coarser grids were also studied with poor quality and unsatisfactory prediction. The left and right boundaries in the spanwise direction of the mainstream channel are set as cell-to-cell match. This is to comply with the requirement of the periodic boundary condition. Two large refinement zones are applied to cover regions from the upstream of the first coolant hole to the downstream of the last hole of the two columns respectively. This refinement aims at better resolving the shear layer and mixing process of the coolant jets and the mainstream. Surface cells are refined close to and in the downstream of the coolant holes for better resolving the separation and the reattachment of the coolant jets. The reason is that the small but highly turbulent near-wall structures are vital to the coolant film distribution and surface ACE. Prism layers are generated from the surface with the first cell height set to satisfy $y^+ \approx 1.0$ based on the mainstream inlet conditions.

4.0 Results and discussion

4.1 Temperature fields

The time-mean temperature field is studied first to show the behaviour of the coolant jet and the mainstream. Fig. 4 illustrates the time-mean temperature contours at a slice through the first column of holes. Overall, the thickness of the coolant film, denoted by the position of the upper shear layer, keeps growing from the first row of coolant holes. Due to the high

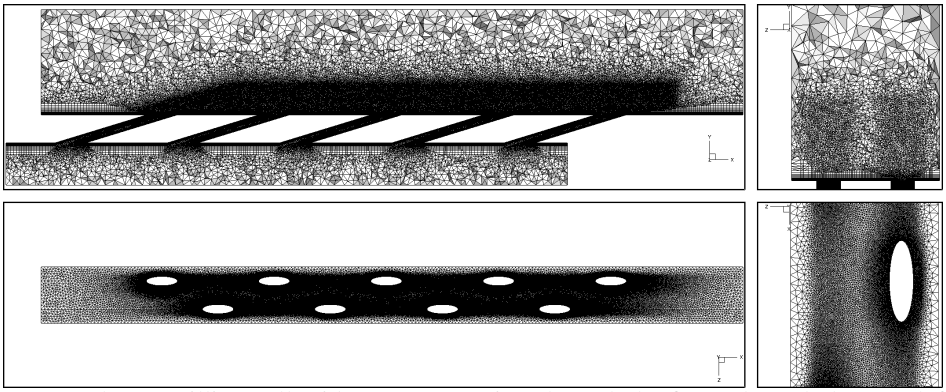

Figure 3: The 18-million-cell grid: a cut-away view through the first column holes (top left), a cut-away view in span (top right), overall view of surface cells (bottom left), enlarged view of surface refinement (bottom right)

momentum ratio (MR = 2.14), the coolant jet from the first hole does not reattach to the plate surface. This results in a high temperature flow occurring near the plate surface downstream the first hole exit. A decreasing near-wall flow temperature is found clearly in the streamwise direction. Also, the coolant flow fully reattaches to the plate surface after the 3rd hole in the figure. It seems that the downstream coolant jets are pressed onto the plate surface by the mixed upstream flow. Furthermore, it can be found that the low temperature jet core of the downstream jets extends further in the streamwise direction. This is possibly due to the increased velocity and reduced temperature of the mixed flow, after a number of coolant jets have been injected to the mainstream.

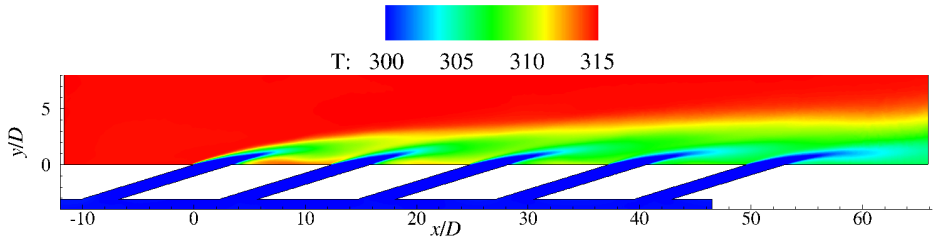

Figure 4: Time-mean temperature contours at a slice through the first column holes

Fig. 5 presents the time-mean temperature contours on the plate surface and selected downstream slices. It can be found that the coolant jets of the first 2 rows are lifted off the plate surface, thus resulting in a low surface ACE. After the 3rd row in the figure, the coolant jets are pressed onto the plate surface by the mixed flow consisted of the mainstream and upstream coolant jets. As a result, the surface temperature is lower since more coolant is reattached to the surface. The spanwise coverage of the coolant film is increased from the 4th row. This is because the spanwise size of the coolant jets are expanded as the jet is pushed towards the plate surface by the upstream mixed flow. The coolant films generated by the two columns of holes are connected in the middle of the span after the 7th row due to this expansion.

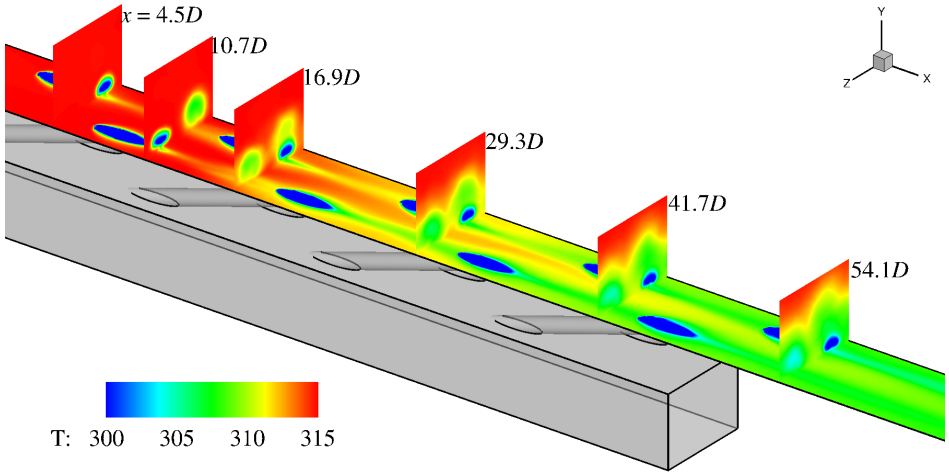

Figure 5: Time-mean temperature contours at surface and selected downstream positions

4.2 Adiabatic cooling effectiveness

Fig. 6 shows contours of the time-mean surface ACE from the simulation. The results of LES clearly demonstrates the development of the coolant film. For the first three rows, the surface ACE after the coolant exit is low due to the small amount of coolant reattaches to the surface. This is the result of the coolant jet penetration into the mainstream at high momentum ratio. From the 4th row, an increasing amount of coolant is reattached to the plate surface and the surface ACE increases significantly. This is because of the downstream coolant jets being forced to reattach to the surface earlier by the mixed flow. The high ACE region along the centreline of the coolant hole trailing edge is captured after the 6th row. This is possibly due to that part of the coolant jet core stays attached to the surface after leaving the trailing edge of the coolant hole exit. It is believed to be another effect of the jet-to-jet interaction in multi-row effusion cooling.

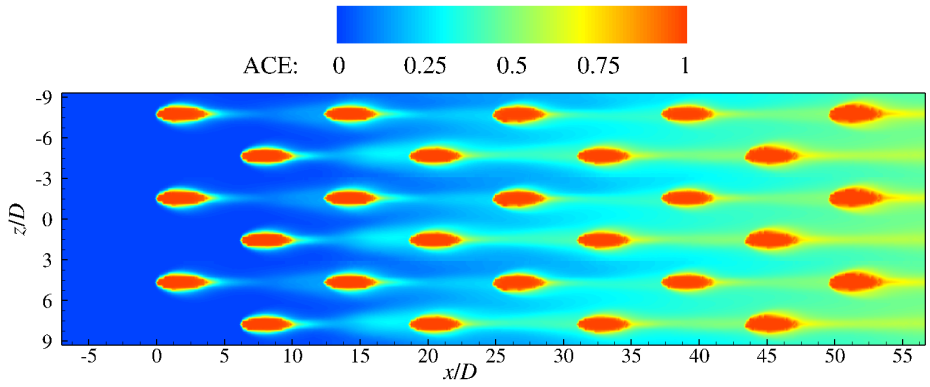

Figure 6: Contours of time-mean surface adiabatic cooling effectiveness at $Tu = 5\%$

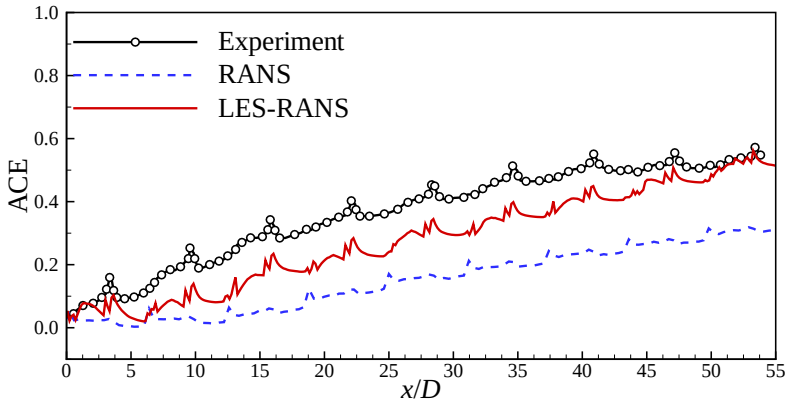

Figure 7: Spanwise-averaged time-mean surface adiabatic cooling effectiveness at $Tu = 5\%$

The spanwise-averaged time-mean ACE profiles are illustrated in Fig. 7. The results agree reasonably well with the measurements in[13], and are much better than those of a RANS calculation. The increasing trend of the surface ACE after each hole is captured well by the hybrid LES approach while the RANS results show a much slower increase. It is found that peaks in the ACE profile occur periodically. The occurrence of these peaks is due to the inclusion of the high ACE region after the trailing edge of each coolant hole during the spanwise averaging process. The ACE values in such regions are higher due to the attached coolant as Fig. 6 illustrates. Hence, peaks occur periodically in the spanwise-averaged ACE profiles. A small underestimation of the surface ACE occurs in the downstream region of $x > 5D$. It indicates that the amount of coolant reattaching to the plate surface is slightly underpredicted. This is possibly due to the not-well-resolved near-wall turbulent structures, which consist of the upstream turbulence, coolant reattachment, jet-mainstream mixing etc. These structures, especially those close to the plate surface, bring coolant jets and mainstream together and thus determine the temperature and coverage of the coolant film near the plate surface. Therefore the extent to which those structures are resolved greatly influences the behaviour of the coolant film and surface ACE.

4.3 Instantaneous flow features

The instantaneous flow features are investigated to study the relation between the turbulent structures and the coolant film distribution on the plate surface. The instantaneous 3D flow structures are illustrated by isosurfaces of λ_2, and coloured by temperature in Fig. 8. Shear layers are formed at the interface between the coolant jet from the first hole in each column and the mainstream. The Kelvin-Helmholtz structures can be observed from the leading edge of the first hole in each column. These structures develop and break down into smaller structures in the downstream region. The hairpin vortices are generated due to the interaction with the plate surface. Smaller turbulent structures are formed downstream when the mixed coolant flow comes across the jet from the next coolant hole. The mixed mainstream flow will push the downstream coolant jets towards the plate surface. This phenomenon has proven to reduce the coolant film temperature attached to the surface and therefore increases the surface ACE. It is also known that the effect becomes more dominant when it moves further to the downstream, since more coolant jets join the mixed flow. Also, a wider spanwise spreading of the coolant

film is obtained as the downstream coolant jet is squeezed to the plate surface.

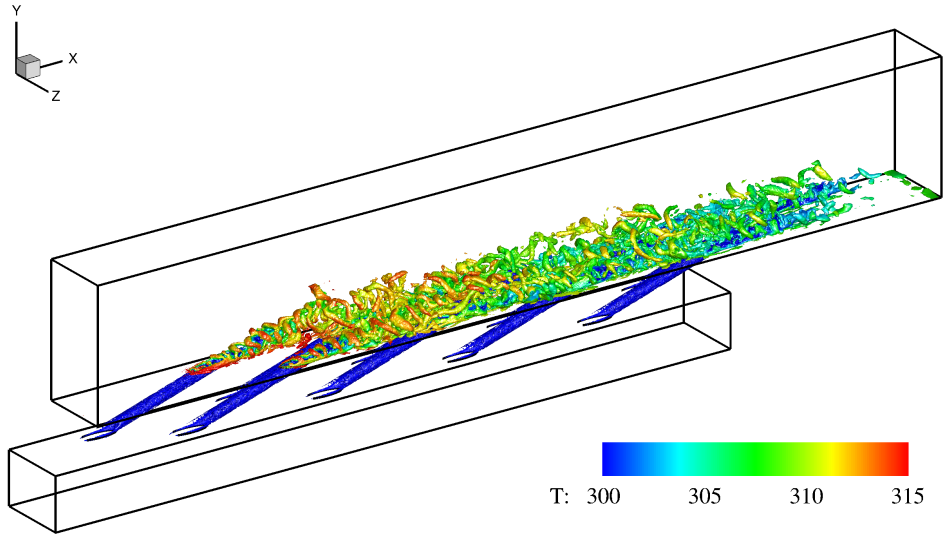

Figure 8: 3D flow structures illustrated by λ_2 and coloured by temperature

The instantaneous temperature contours and spanwise vorticity on a slice through the first column of holes are presented in Fig. 9 and Fig. 10 respectively. The turbulent inflow, jet-mainstream shear layers and smaller structures caused by the separation and reattachment of the coolant flow are clearly illustrated in the contours of vorticity. The effects of these structures on the near-wall flow temperature can be studied from the contours of temperature. As Fig. 9 shows, the shear layer formed at the leading edge of the first hole is broken down by the inflow turbulence not far downstream the trailing edge of the coolant hole. Thus the coolant jet penetration into the mainstream is shortened. This leads to a faster reattachment of the coolant jet to the plate surface, which would reduce the near-wall flow temperature. However, the inflow turbulence also enhances the mixing of the coolant jets with the hot mainstream. As a result of the combination of these two effects, the surface ACE downstream the first 2 holes in Fig. 9 remains at a low level. Moreover, the early breakdown of the coolant jet also results in a reduced force in pushing the coolant jet from the downstream coolant hole to the plate surface in this multi-row configuration. Therefore, the surface ACE after the 2nd and 3rd coolant holes is still dominated by the breakdown effect of the inflow turbulence. As pointed out by the surface ACE distribution, the squeezing effect of the mixed mainstream flow becomes dominant only after the 6th row.

The instantaneous temperature and streamwise vorticity contours at selected downstream positions are shown in Fig. 11 and Fig. 12 respectively. It is found from the vorticity contours that the two shear layers die out soon after the trailing edge of the first and second row of holes. Moreover, the coolant jets from the first and second coolant holes break up before they reach the downstream hole. This confirms the finding that the inflow turbulence breaks down the coolant jet early. It is also proved by the temperature contours that the squeezing effect by the upstream mixed coolant flow starts only after the 4th row. The inflow turbulence in the mainstream is found to exist throughout the channel, though the intensity level drops towards

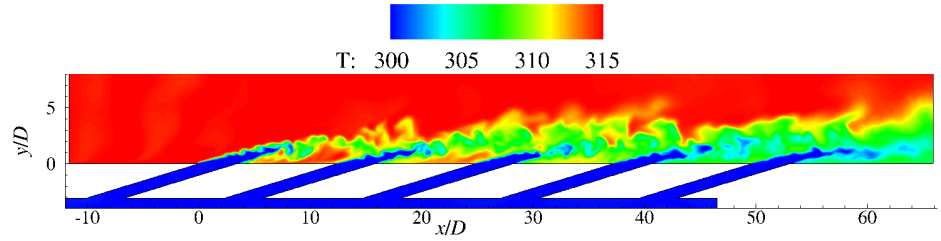

Figure 9: Instantaneous contours of temperature through the first column holes

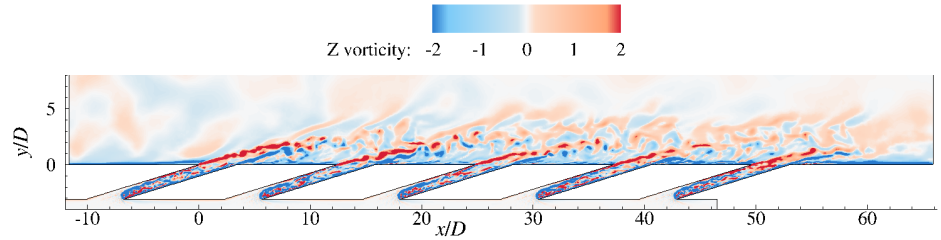

Figure 10: Instantaneous contours of non-dimensional spanwise vorticity through the first column holes

the downstream. Furthermore, the near-wall structures downstream the first row vanishes quickly in the streamwise direction due to the early breakdown of the coolant jet. However, the near-wall structures stay active further downstream the coolant exit in the downstream rows as the squeezing effect enhances the flow mixing and reattachment in the near-wall region.

4.4 Energy spectra

The unsteady features of the flow field are also examined by the power spectra in the upper shear layer and on the wall downstream of the first column coolant holes. Fig. 13 shows a sketch of the probe positions to extract the time signal for the spectral analysis. Two groups of probes are considered. The first group is located in the upper shear layer $y = 1D$ at the trailing edge of each coolant exit. The second group is placed on the plate surface and at the same streamwise position as the first group.

The spectra of turbulence kinetic energy (TKE) and pressure fluctuation in the upper shear layer are shown in Fig.14. The TKE spectra in the shear layer of all 5 holes follow the Kolmogorov's $-5/3$ law in the inertial subrange. It demonstrates that the turbulent structures in the upper shear layer is fully developed. A few modes can be found in the spectra, especially from that of the 1st hole. One of the modes is clearly illustrated by the spectra of pressure fluctuation at about 8000 Hz. This frequency is considered to be the major frequency of the shear layer instability. However, this peak diminishes in the spectra of the downstream holes because the small turbulent structures in mixed flow destroys the potential shear layer that might be formed between the mixed flow and downstream coolant jets.

The spectra of temperature in the upper shear layer ($y = 1D$) and on the wall are presented in Fig. 15. It is clearly shown that the temperature spectra both in the shear layer and on

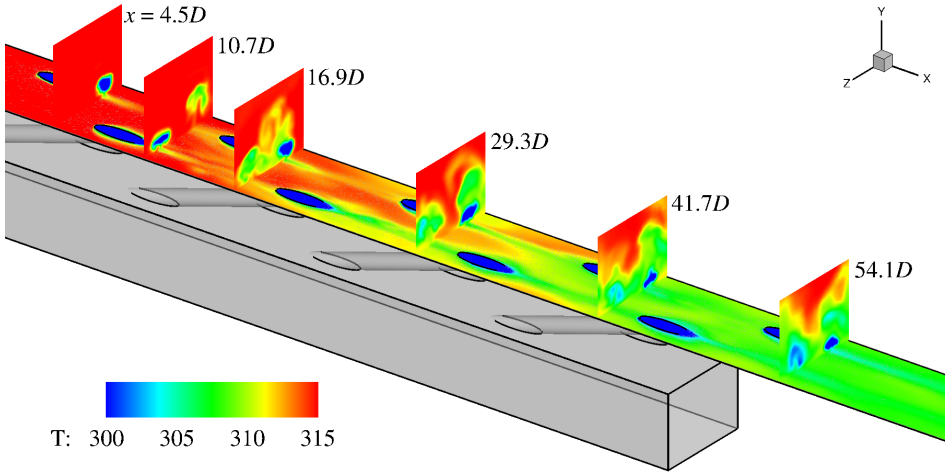

Figure 11: Instantaneous contours of temperature at surface and selected downstream positions

the wall have a major peak frequency at about 8000 Hz, which is consistent with the shear layer instability frequency. The second and third peaks are also found in the spectra of the first hole both in the upper shear layer and on the wall. This is because the upstream flow for the first coolant jet does not contain any mixed coolant flow. Therefore the instability in the shear layer is purely generated by the mixing of coolant jet and mainstream. Moreover, the presence of lower shear layer also brings a few frequency modes to the temperature spectrum on the wall. However, the frequency modes diminish in the spectra at downstream positions. This is due to the fact that the coolant injected to the mainstream from the upstream holes leads to a reduced temperature in the mixed flow. Therefore, the temperature fluctuation becomes less in the position where the upper shear layer should be. As for the spectra on the wall, the coolant jets from the downstream holes are squeezed to the plate surface so that the temperature fluctuation is restricted and the frequency modes are diminished.

5.0 Conclusions

Numerical investigations have been successfully carried out on a multi-row effusion cooling configuration under representative combustor conditions. Simulation was conducted using a hybrid LES-RANS approach on a coarse 18-million-cell grid. Reasonable agreement has been obtained in the surface ACE distribution and the spanwise-averaged ACE between the numerical results and the measurements.

Investigations have been carried out to study the relation between the flow features, especially the turbulent structures and the coolant film distribution on the surface. It was found that the inflow turbulence resulted in an early breakdown of the shear layer as well as the coolant jet at the first 2 rows of holes. The surface ACE distribution downstream of the first several rows was therefore influenced by the inflow turbulence. After the 5th row, the effects of mainstream turbulence were diminished. The coolant film distribution and the surface ACE were dominated by the squeezing effect of the mixed mainstream flow. A major frequency of

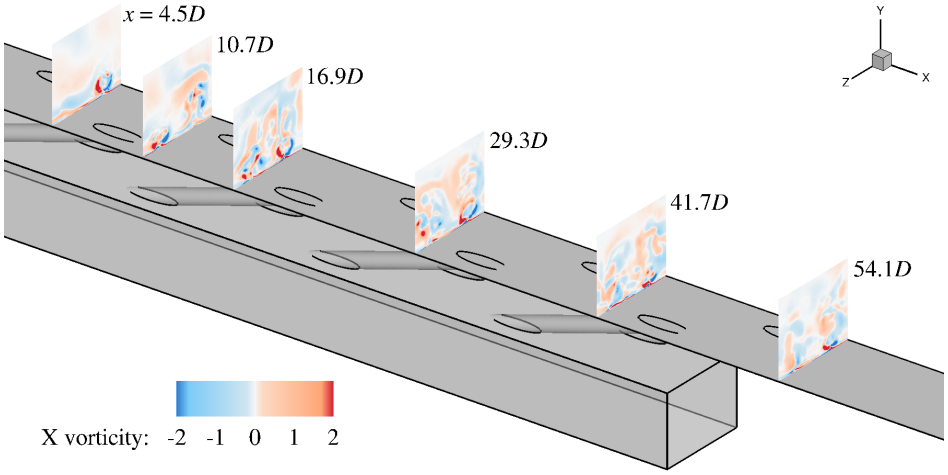

Figure 12: Instantaneous contours of non-dimensional streamwise vorticity at surface and selected downstream positions

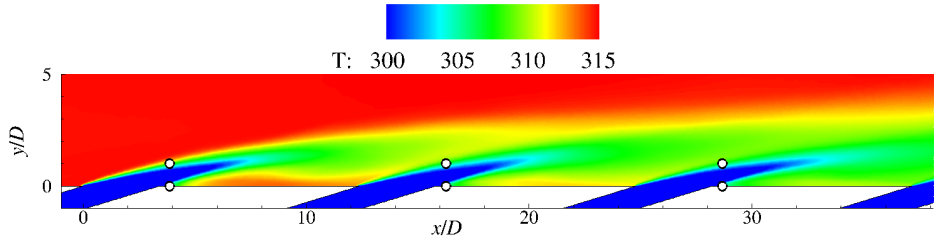

Figure 13: A sketch showing the location of the probes for the spectral analysis

the shear layer instability is found at a Strouhal number of about $St = 0.65$. Although this frequency diminishes in the downstream shear layer due to the highly turbulent mainstream after a number of coolant jets were injected. However, this frequency modes, although very weak, can still be found in the downstream close to the plate surface.

Acknowledgements

The authors would like to acknowledge the use of the “Hydra” High Performance Computing System at Loughborough University. Financial and technical support from the Department of Aeronautical and Automotive Engineering and the Rolls-Royce UTC at Loughborough University made this work possible.

NOMENCLATURE

c_p	specific heat capacity at constant pressure
D	coolant hole diameter
d	standard wall distance

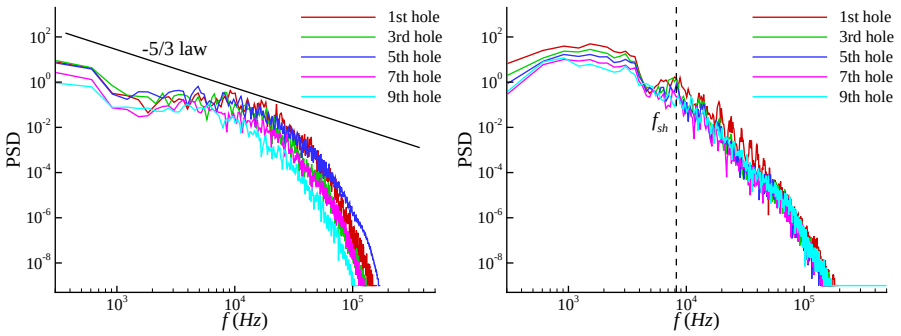

(a) TKE (b) Pressure fluctuation

Figure 14: Power spectral density of (a) turbulence kinetic energy and (b) pressure fluctuation in the shear layer

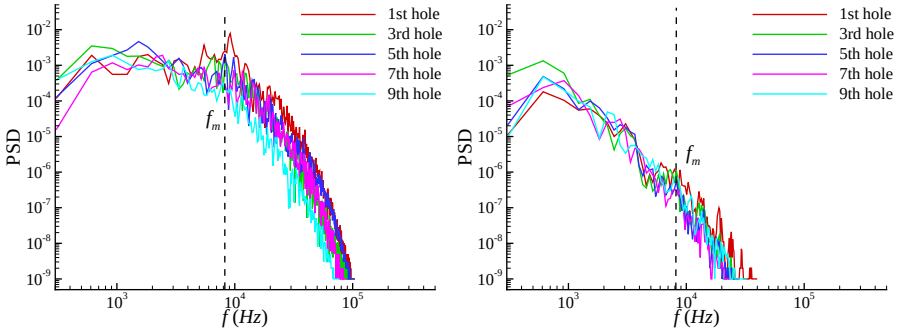

(a) Shear layer (b) Wall

Figure 15: Power spectral density of temperature (a) in the shear layer and (b) on the wall

d_c	RANS cut-off distance
$\widetilde{d}$	modified wall distance
E	total energy
e	internal energy
$\mathbf{F}$	flux vector
$\mathbf{F}^{inv}$	inviscid flux vector
$\mathbf{F}^{vis}$	viscous flux vector
L_T	turbulent length-scale
Pr, Pr_T	Prandtl number, turbulent Prandtl number
p	static pressure
$\mathbf{Q}$	vector of primitive variables, $(\rho, \rho u_i, E)^T$
q	heat flux density
R	gas constant
Re	Reynolds number
S_{ij}	strain rate tensor

T	temperature
t	dimensional time
Tu	turbulence intensity
U	averaged velocity
u, v, w	velocity components in x, y, z direction, also used in u_i form
x, y, z	Cartesian Coordinates, also as x_i
y^+	non-dimensional wall distance

Greek Symbol

γ	upwinding control parameter
Δ	grid spacing
δ_{ij}	Kronecer delta
ε	weighting of LES
κ, κ_T	thermal conductivity
μ, μ_T	molecular viscosity, eddy viscosity
ρ	density
τ_{ij}	stress tensor

REFERENCES

1. Sinha, A.K., Bogard, D.G and Crawford, M.E. Film-Cooling Effectiveness Downstream of a Single Row of Holes with Variable Density Ratio, *J. Turbomach.*, 1991, **113**, (3), pp 442-449.
2. Pietrzyk, J.R., Bogard, D.G. and Crawford, M.E. Effects of Density Ratio on the Hydrodynamics of Film Cooling, *J. Turbomach.*, 1990, **112**, (3), pp 437-443.
3. Goldstein, R.J., Eckert, E.R.G. and Burggraf, F. Effects of Hole Geometry and Density on Three-Dimensional Film Cooling, *Int. J. Heat Mass Transf.*, 1974, **17**, pp 595-607.
4. Goldstein, R.J. and Yoshida, T. The Influence of a Laminar Boundary Layer and Laminar Injection on Film Cooling Performance, *J. Heat Transf.*, 1982, **104**, (2), pp 355-362.
5. Walters, D.K. and Leylek, J.H. A Systematic Computational Methodology Applied to a Three-Dimensional Film-Cooling Flowfield, *J. Heat Transfer*, 1997, **116**, pp 358-368.
6. Azzi, A. and Jubran, B.A. Numerical Modeling of Film Cooling from Short Length Stream-Wise Injection Holes, *Heat Mass Transf.*, 2003, **39**, pp 345-353
7. Li, X., Ren, J. and Jiang, H. Application of Algebraic Anisotropic Turbulence Models to Film Cooling Flows, *Int. J. Heat Mass Transfer*, 2015, **91**, pp 7-17
8. Tyagi, M. and Acharya, S. Large Eddy Simulation of Film Cooling Flow from an Inclined Cylindrical Jet, *J. Turbomach.*, 2004, **125**, pp 737-742
9. Liu, K. and Pletcher, R.H. Large Eddy Simulation of Discrete-Hole Film Cooling in a Flat Plate Turbulent Boundary Layer, *38th AIAA Thermo-physics Conference*, 2005, Toronto, Canada, AIAA paper No. 2005-4944
10. Renze, P., Schröder, W. and Meinke, M. Large-Eddy Simulation of Film Cooling Flows with Variable Density Jets, *Flow Turbul. Combust.*, 2008, **80**, (1), pp 119-132

11. Ziefle, J. and Kleiser, L. Numerical Investigation of a Film-Cooling Flow Structure: Effect of Crossflow Turbulence, *J. Turbomach.*, 2013, **135**, (4), pp 041001:1-12

12. Martin, D. Effects of High Intensity, Large-scale Free-stream Turbulence on Combustor Effusion Cooling, Ph.D. Thesis, 2013, Loughborough University, Loughborough, UK

13. Krawciw, J., Martin, D. and Denman, P. Measurement and Prediction of Adiabatic Film Effectiveness of Combustor Representative Effusion Arrays, *ASME Turbo Expo 2015*, Montreal, Canada, ASME paper No. GT2015-43210

14. Menter, F.R., Kuntz, M. and Langtry, R. Ten Years of Industrial Experience with the SST Turbulence Model, *Turbulence, Heat and Mass Transfer 4*, 2003, pp 625–632

15. Xia, H., Tucker, P.G. and Eastwood, S. Large-eddy Simulations of Chevron Jet Flows with Noise Predictions, *Int. J. Heat Fluid Fl.*, 2009, **30**, (6), pp 1067-1079

16. Xia, H. and Tucker, P.G. Numerical Simulation of Single-stream Jets from a Serrated Nozzle, *Flow Turbul. Combust.*, 2012, **88**, (1), pp 3-18

17. Chen, X. and Xia, H. A Hybid LES-RANS Study on Square Cylinder Unsteady Heat Transfer, *Int. J. Heat Mass Transf.*, 2017, **108**, (A), pp 1237-1254

18. Jarrin, N. Synthetic inflow boundary conditions for the numerical simulation of turbulence, Ph.D. Thesis, 2008, University of Manchester, Manchester, UK